Journal of Materials Chemistry A

Novel two-dimensional semiconductor SnP3: high stability, tunable bandgaps and high carrier mobility explored by first-principles calculations

Journal:	*Journal of Materials Chemistry A*
Manuscript ID	TA-ART-03-2018-002494.R1
Article Type:	Paper
Date Submitted by the Author:	29-Apr-2018

Complete List of Authors:	Sun, Songsong; Southwest Jiaotong University, school of physical science and technology Meng, Fanchen; Clemson University, Department of Physics and Astronomy Wang, Hongyan; Southwest Jiaotong University, ; Wang, Hui; Southwest Jiaotong University Ni, Yuxiang; Southwest Jiaotong University, School of Physical Science and Technology

ROYAL SOCIETY OF CHEMISTRY

ARTICLE TYPE

Cite this: DOI: 10.1039/xxxxxxxxxx

Novel two-dimensional semiconductor SnP_3: high stability, tunable bandgaps and high carrier mobility explored by first-principles calculations†

Songsong Sun,[a] Fanchen Meng,[b] Hongyan Wang,[a] Hui Wang,[a] and Yuxiang Ni*[a]

Received Date
Accepted Date

DOI: 10.1039/xxxxxxxxxx

www.rsc.org/journalname

We propose a novel two-dimensional crystal based on a layered metallic bulk SnP_3 by first-principles calculations. The obtained low cleavage energy of SnP_3 monolayer and bilayer imply the possibility of their exfoliation from layered bulk SnP_3 experimentally. The SnP_3 monolayer and bilayer are structurally stable with 0.72 eV and 1.02 eV indirect band gaps respectively at HSE06 functional level. Tunable bandgaps can be achieved by strain engineering. With a compressive strain of 4%, the valence band maximum of SnP_3 bilayer varies from the high symmetry point K to point Γ, resulting in the transform from indirect to direct semiconductor. Analogy to phosphorene, remarkably high carrier mobilities are predicted for SnP_3 monolayer, which is several times higher than that of GeP_3 monolayer. The holes mobilities of SnP_3 bilayer can reach as high as 10^4 $cm^2V^{-1}s^{-1}$. Moreover, the excellent absorption coefficient in the range of solar spectrum were predicted. These results qualify SnP_3 monolayer and bilayer as promising novel 2D materials for applications in microelectronics, optoelectronics and field-effect transistors.

1 Introduction

The explorations of two-dimensional (2D) materials have come into a rapid development period with the discovery of the 2D carbon allotrope graphene in 2004.[1] Graphene has rapidly become one of the hotspots in materials science domain due to its unique chemical and physical properties. Although graphene can offer ultrahigh carrier mobility, which is more than 10^5 $cm^2V^{-1}s^{-1}$,[2] the intrinsic semimetallic features and the zero band gap have greatly limited its applications in microelectronic devices, such as field-effect transistors (FET).

However, the successful exfoliation of graphene greatly motivated the exploration of 2D structures, such as transitional metal dichalcogenides (TMDs),[3–5] hexagonal BN,[6–8] silicene,[9] phosphorene,[10] germanane,[11], group-*IV* monochalcogenides (MX, M=Ge, Sn; X=S, Se)[12] and MXenes.[13] These 2D structures possess several properties rivaling and surpassing those of graphene. Unlike graphene, MoS_2 monolayer is a semiconductor with a direct bandgap of 1.80 eV[14]and the carrier mobility in excess of 200 $cm^2V^{-1}s^{-1}$,[15] which make it a promising candidate for FET and optoelectronic devices. Compared with MoS_2 monolayer, phosphorus presents a moderate direct bandgap[16] and highly anisotropic hole mobility of at least 10^3 $cm^2V^{-1}s^{-1}$.[17] Therefore, phosphorene holds great promise to replace silicon in microelectronics. Recently, GeP_3 monolayer and bilayer were theoretically proposed[18] as a novel 2D structure with tunable indirect bandgaps, high carrier mobilities and excellent absorption coefficient of solar energy, which can also be exfoliated from layered bulk GeP_3. It is also reported that Indium triphosphide (InP_3) possesses an indirect band gap of 1.14 eV and a high electron mobility of 1919 $cm^2V^{-1}s^{-1}$, which could be strongly manipulated with strain engineering.[19] The monolayer BP_3, which is a semiconductor with an indirect band gap (0.77 eV) within the HSE06 calculation, exhibits a high electron mobility ($\sim 4.6\times10^4 cm^2V^{-1}s^{-1}$), which is comparable to the experimental value of graphene.[20] Yang et al. reported that new 2D silicon crystals can be obtained by functionalizing silicene with silicon atom, dimer, or chains, which exhibit lower formation energy than that of silicene. Meanwhile, the 2D silicon crystals possess ultrahigh carrier mobility up to 1.7 $\times10^5$ $cm^2V^{-1}s^{-1}$ and 1.3×10^4 $cm^2V^{-1}s^{-1}$1 at room temperature for electron and hole, respectively.[21]

On the other hand, a layered material composed of Sn and P with stoichiometry SnP_3 has already been synthesized and investigated in 1970s.[22] Analogous to GeP_3, SnP_3 also possesses the puckered arsenic-type honeycomb in ABC stacking, as well as the superconductive property. Thus, the exfoliation of the monolayer and bilayer SnP_3 should be achievable. In this study, we identify the SnP_3 monolayer and bilayer as novel 2D semiconductors by using first-principle calculations. We first assess the dynamical and chemical stability of the SnP_3 monolayer and bilayer, accord-

[a] School of Physical Science and Technology, Key Laboratory of Advanced Technology of Materials (Ministry of Education), Southwest Jiaotong University, Chengdu 610031, China. E-mail: yuxiang.ni@swjtu.edu.cn
[b] Department of Physics and Astronomy, Clemson University, Clemson 29634, USA.

ing to the phonon dispersion curves and work function, respectively. The possibility and feasibility of exfoliating the monolayer and bilayer SnP_3 from its layered bulk form were explored. Then we systematically investigated the electronics properties of SnP_3 monolayer and bilayer, under both free-standing and strained conditions. Furthermore, the intrinsic carrier mobility of SnP_3 monolayer and bilayer was evaluated according to the deformation potential theory. Finally, the optical absorption coefficients were presented. This study should shed light on the investigation of 2D SnP_3 materials, and evoke more attention for exploring their versatile applications in microelectronics, optoelectronic and FET devices.

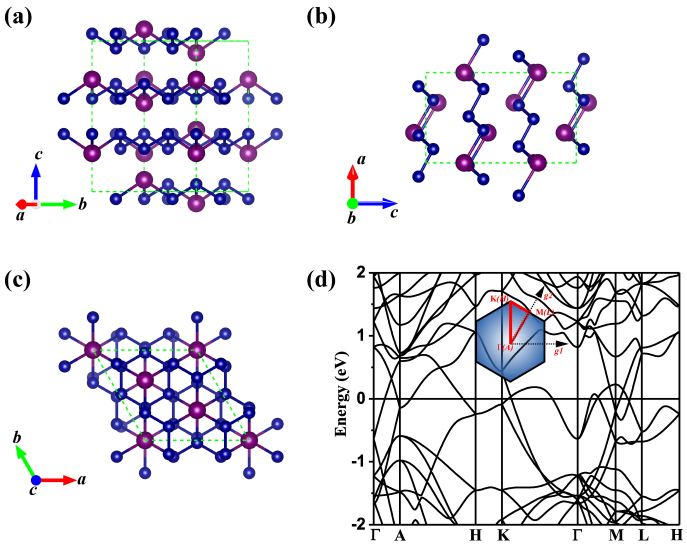

Fig. 1 Side (a),(b),and top (c) views of optimized unitcell of bulk SnP_3. Purple and blue balls represent Sn and P atoms, respectively. (d) The band structure of bulk SnP_3 unitcell calculated at the PBE level. Inserted is the first Brillouin zone with high symmetric k points: Γ (0,0,0), A (0,0,0.5), H (-0.333,0.667,0.5), K (-0.333,0.667,0), M (0,0.5,0), and L (0,0.5,0.5).

2 Theoretical and computational details

All first-principles calculations were performed using the plane-wave based density functional theory (DFT) as incorporated in the Vienna *ab initio* simulation package (VASP)[23,24]. The electron-ion interaction was described by the projector augmented wave (PAW) method,[25]and the plane-wave cut-off energy was set as 500 eV. The atomic optimization and electronic structure calculations were implemented using the generalized gradient approximation (GGA) method with the Perdew-Burke-Ernzerhof (PBE) exchange-correlation functionals.[26] In particular, band structures were obtained based on the Heyd-Scuseria-Ernzerhos hybrid functional (HSE06)[27,28] to correct the underestimated bandgaps in PBE. The van der Waals (vdW) interactions were corrected by using the DFT-D2 approach.[29] The Brillouin zone was sampled with 15× 15 × 1 Monkhorst-Pack scheme[30] grid during geometry optimization of the unit cell and 25 × 25 × 1 grid for the electronic structure calculation. The vacuum layer was set as ∼ 20 Å to minimize the interlayer interaction between periodic layers. To completely relax all atoms in the unit cell, the convergence benchmark for the force and total energy were chosen to be 0.01 eV/Å and 1×10^{-5} eV, respectively. Phonon band dispersions were calculated by using the PHONOPY package[31] with the density perturbation functional theory (DPFT), where a 5×5×1 K-mesh was used. Ab initio molecular dynamics (AIMD) simulations were performed to check the thermal stability of the structures using the Nosé-Hoover thermostat.[32]

3 Results and discussion

3.1 Structures and stability of SnP_3 monolayer and bilayers

The geometric structure of bulk SnP_3 (Fig. 1) possesses $R\bar{3}m$ space group, which is of the same symmetry as bulk GeP_3. The optimized lattice parameters of bulk SnP_3 are $a = b = 7.458$ Å, and $c = 10.772$ Å, which are in agreement with the experimental data.[22] It can be seen that the layered bulk (Fig. 1(a)) SnP_3 structure has a puckered configuration (Fig. 1(b)) along the a direction, which is analogical to that of blue phosphorene. Obviously, the atoms of each layer of bulk SnP_3 are located in two adjacent hexagonal planes (Fig. 1(c)), while each Sn atom forms three Sn-P bonds with three neighboring P atoms, and each P atom forms two P-P bonds and one Sn-P bond with neighboring P and Sn atoms, respectively. As shown in Fig. 1(d), the bulk SnP_3 presents metallic character due to the bands cross the Fermi level.

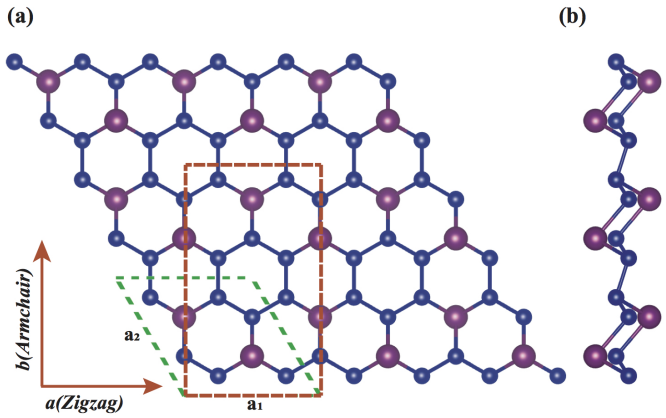

Fig. 2 Top (a) and side (b) views of the atomic structure of monolayer SnP_3 in 3 × 3 × 1 supercell. The green and red dashed lines indicate the unitcell (defined by a_1 and a_2) and the rectangular supercell (defined by *a* and *b* along the zigzag and armchair directions), respectively.

Fig. 2 depicts the optimized structure of SnP_3 monolayer, which is obtained by exfoliating from the layered bulk SnP_3. The unit cell is indicated by rhombus marked with green dashed lines, with the lattice parameters of $a_1 = a_2 = 7.160$ Å. Compared with bulk SnP_3, the puckered configuration of SnP_3 monolayer is more pronounced (Fig. 2(b)), resulting in the shrinkage of the lattice parameters (as illustrated in Table. 1). The shrinkage of lattice parameters of monolayer SnP_3 changes the bond lengths and bond angles compared with their bulk counterparts, which is also the driving force for its metallic to semiconductive transition. For the sake of convenience, the rectangular supercell (marked by the red dashed lines) was constructed to investigate the carrier mobility

along the zigzag and armchair directions.

Table 1 The calculated lattice parameters (lattice constant *a*, bond length for Sn-P and P-P, angle P-P-P)of SnP_3 bulk, monolayer, bilayer and trilayer, respectively

unitcell type	a (Å)	Δ_{Sn-P}(Å)	Δ_{P-P}(Å)	$\angle_{P-P-P}$
Monolayer	7.160	2.710	2.171	111.1
Bilayer	7.222	2.619	2.218	99.4
Trilayer	7.283	2.692	2.227	98.8
Bulk	7.402	2.670	2.231	99.1

Before investigating the electronic properties of monolayer and bilayer SnP_3, we estimated its dynamic stability by calculating their phonon dispersion curves (as shown in Fig. 3(a) and (b)). It can be inferred that the monolayer and bilayer SnP_3 are kinetically stable since no appreciable imaginary phonon modes are found.[33,34] Secondly, the thermal stability of SnP_3 monolayer is examined by performing AIMD simulations using the canonical ensemble at room temperature (300K) with a time step of 1 fs. The total potential energy is stabilized at around 2 ps, and no structural reconstruction was observed at the end of the simulation (12 ps). More information can be found in the Supplementary Information. The results suggest that the SnP_3 monolayer is thermally stable.[35,36] Moreover, the work function of monolayer SnP_3 is higher (4.87 eV) than that of phosphorene (4.25 eV) at the PBE level, which indicates that it is also chemically stable.

In general, the main techniques to access the monolayer and few-layer structures from the layered bulk materials are liquid phase exfoliation[37] and mechanical cleavage.[38] To evaluate the possibility of exfoliating monolayer and bilayer structures from layered bulk SnP_3, we calculated the cleavage energy of SnP_3 monolayer and bilayer with a five-layer slab model. The variations in total energy according to the separation distance d between the fixed four (three) layers and the flexible one (two) layer(s) were calculated to simulate the natural process of exfoliation as shown in Fig. 3(b). With the increase of d, the cleavage energy gradually increases and finally converges to constant values of ~ 0.57 and $0.38\ J/m^2$ for SnP_3 monolayer and bilayer, respectively. For comparison, the cleavage energy of some layered materials estimated using DFT, like graphene,[39] BiI_3,[40] GeS_2,[41] NaSnP,[42] GeP_3,[18] and Ga_2N[43] are 0.36, 0.43, 0.52, 0.81, 0.91, and $1.09\ J/m^2$, respectively. Therefore, the SnP_3 monolayer and bilayer are feasible to be exfoliated from the layered bulk due to their cleavage energies are in the same range with the above mentioned layered materials.

3.2 Electronic properties of SnP_3 layers

Having verified the stability and identified the possibility of exfoliation from layered bulk, the orbital-projected band structures were computed to better understand the particular electronic properties of the monolayer and bilayer of SnP_3 with PBE functional. As shown in Fig. 4(a) and (b), both of them are indirect bandgap semiconductors with bandgaps of 0.43 eV and 0.61 eV for monolayer and bilayer, respectively. In both SnP_3 monolayer and bilayer, the valence band maximum (VBM) is located at K point, while the conduction band minimum (CBM) sits at Γ point. The more elaborate HSE06 functional yields similar band structures shapes with wider bandgaps of 0.72 and 1.02 eV for SnP_3 monolayer and bilayer. According to the orbital-projected band structure presented in Fig. 4(a) and (b), the VBM of SnP_3 monolayer mainly consists of the p_z-orbitals of P atoms and the p_z-orbitals of Sn atoms, while the CBM of SnP_3 monolayer is mainly from the p_z-orbitals of P atoms. The partial charge densities corresponding to the VBM and CBM of SnP_3 monolayer plotted in Fig. 4(c) and (d) are in agreement with the orbital-projected band structures analyses. For example, the VBM of SnP_3 monolayer mainly locates at the P atoms, whereas the CBM appears around the P and Sn atoms.

It is interesting to note that SnP_3 triplelayer starts to exhibit metallic property, according to the band structure shown in Fig. 4(e). There are two possible reasons for this transition. Firstly, the structure of SnP_3 can be described as a layer structure related to the As-type structure in which the corrugated layers are composed of puckered P_6 rings,[22] as shown in Fig. 1. The layers thus formed are stacked upon one another perpendicular to the c axis so that a distorted octahedral environment of P atoms is formed around each of the Sn atoms, which results in significant puckering and a pseudo-Jahn-Teller distortion.[44] We calculated the interlayer interaction from the multilayer to bilayer and the results (see Fig. S1 of the Supplementary Information) illustrate that the interlayer interaction for SnP_3 systems decreases from tetralayer to bilayer. Thus, we believe that the dependence of the interlayer interaction on the layer thickness most likely plays an important role in the metal to semiconductor transition in the SnP_3 layered systems.[45] Meanwhile, the quantum confinement effect may be another factor that affects the electronic structure transition. When the multilayer with metallic character reduced to semiconductive bilayer, the conduction bands shift towards the vacuum level.

Since Sn is a heavy element, which possesses the valence electrons $5s^25p^2$, the spin-orbital-coupling(SOC) effect may affect the electronic properties of the SnP_3 monolayer and bilayer. The band structure of SnP_3 monolayer with and without SOC were calculated and shown in Fig. 4(f). It can be seen that the VBM and CBM of the SnP_3 monolayer substantially coincide with each other regardless of SOC effect at the PBE functional level. As the p-orbitals of P atoms are the main contributors to the VBM and CBM, the SOC effect is not strong enough to influence the electronics properties of the 2D SnP_3 in this study, and it can be neglected in the following discussions.

3.3 Band edge tuning via compressive and tensile strains

A large number of experimental and theoretical studies such as germanane,[46] WX_2 (X= S, Se, Te),[47–49] Graphene Allotrope,[50] Tinselenidene,[51] and Germanium[41] have demonstrated that the geometric, mechanical, electronics and transport properties of 2D structures can be effectively modified via strain engineering. Compressive or tensile strains are helpful in solving the ineluctable lattice parameters mismatch problem in the practical applications, and the controllable band structures brought by strain engineering broadens the applications of 2D materials. To

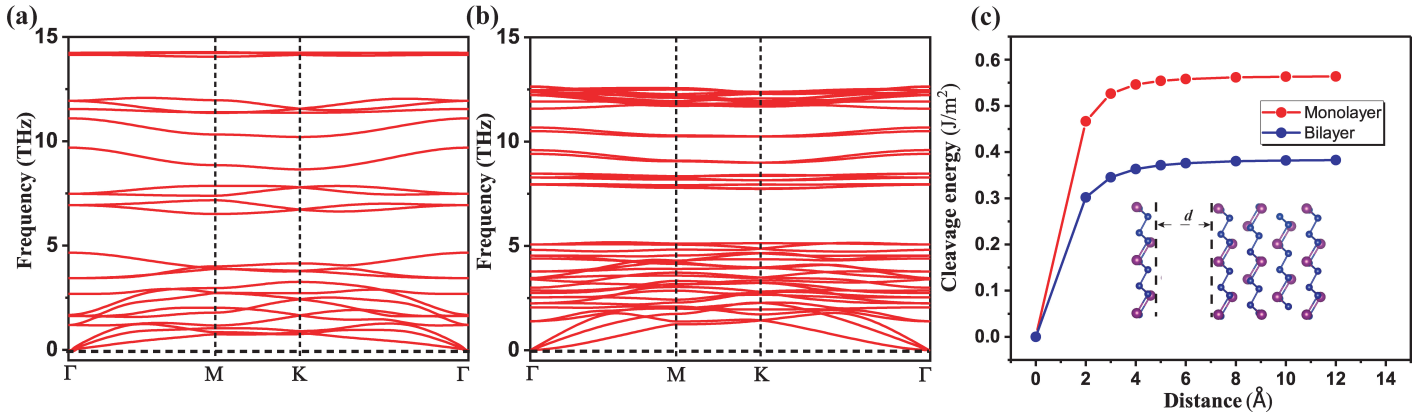

Fig. 3 The phonon dispersion for SnP_3 monolayer (a) and bilayer (b) with 4 × 4 × 1 supercells. (c) Cleavage energy as a function of the separation distance between SnP_3 monolayer/bilayer and the remainder of a five-layers slab model. The distance of zero corresponds to the equilibrium geometry of the five-layer slab.

Table 2 Carrier effective masses m^*_{zig} and m^*_{arm}, in-plane stiffness of 2D structure C^{2D}_{zig} and C^{2D}_{arm}, the deformation potential constant E^{zig}_d and E^{arm}_d, and the carrier mobility μ^{2D}_{zig} and μ^{2D}_{arm} of monolayer and bilayer SnP_3 along the zigzag and armchair directions at room temperature. Data in the parentheses denote the corresponding values of GeP_3 taken from Ref. 17.

Models	Carrier type	m^*_{zig}/m_0	m^*_{arm}/m_0	C^{2D}_{zig} (N/m)	C^{2D}_{arm} (N/m)	E^{zig}_d (eV)	E^{arm}_d (eV)	μ^{2D}_{zig} $(cm^2V^{-1}s^{-1})$	μ^{2D}_{arm} $(cm^2V^{-1}s^{-1})$
Monolayer	electron	0.90	0.90	32.96	33.00	3.51	3.52	197.69 (40)	207.30 (70)
	hole	1.64	0.72	32.96	33.00	1.55	1.55	172.68 (14)	359.25 (190)
Bilayer	electron	0.20	0.20	93.02	92.95	2.09	2.06	1.66 (1.25)×10^3	1.74 (8.84)×10^3
	hole	0.71	0.82	93.02	92.95	0.45	0.32	1.11×10^4 (4630)	1.15×10^4 (8480)

gain more insights, we investigated the band structure of SnP_3 monolayer and bilayer with respect to biaxial mechanical strains, and the results are shown in Fig. 5. All the applied biaxial strains here are in the elastic region, which is confirmed by the quadratic dependence of the strained energy on the applied strains, as is shown in Figure. S3 of the Supplementary Information.

The applied mechanical strain δ is defined as $\delta = \Delta l/l_0$, in which l_0 is the equilibrium lattice constant and Δl is the change of the lattice constant. As depicted in Fig. 5(a), the bandgap of SnP_3 monolayer decreased progressively with increasing compressive strain, and it becomes metalic at a compressive strain of -6%. The monolayer bandgap first broadened with the increase of tensile strain (Fig. 5(b)). After reaching the largest value of 0.63 eV, the bandgap begins to decrease when the tensile strain is larger than 8%. Meanwhile, the CBM moves from gamma point to M point, resulting in an indirect to quasi-direct band gap transition. For bilayer SnP_3 under compressive strains, the bandgap continuously decrease, similar to the behaviors of monolayer. Interestingly, with a compressive strain of 4%, the VBM of SnP_3 bilayer changes from the high symmetry point K to point Γ, which leads to the transition of indirect to direct semiconductor. Fig. 5(d) shows that the band gap of SnP_3 bilayer decreases with the increase of tensile strain. The above results indicate that the electronic properties of SnP_3 monolayer and bilayer can be flexibly tuned via strain engineering, which may broaden their practical applications such as in flexible electronics.

3.4 Carrier mobilities of SnP_3 monolayer and bilayers

To further understand the potential applications of SnP_3 monolayer and bilayer in microelectronic devices or as photocatalysts, we systematically calculated their carrier mobilities, which provides information of the carriers transfer capacity along different directions. According to the deformation potential (DP) theory initially proposed by Bardeen and Shockley,[52] the carrier mobility of 2D materials can be described by the following expression,[53–56]

$$\mu = \frac{2e\hbar^3 C^{2D}_\alpha}{3k_B T|m^*|^2(E^\alpha_d)^2}, \quad (1)$$

where e is the electron charge, $\hbar$ is the reduced Plank constant, k_B is the Boltzmann constant, m^* is the effective mass of electrons and holes, and T is the temperature (set to be 300K). m^* can be calculated using the following equation:

$$\frac{1}{m^*} = \frac{1}{\hbar^2}\frac{\partial^2 E(k)}{\partial k^2}, \quad (2)$$

where k and $E(k)$ are the wave vector and the energy corresponding to k, respectively. As listed in Table. 2, the electrons effective masses of SnP_3 monolayer are about three times smaller than the holes effective masses along both zigzag and armchair directions, suggesting that the transfer of the electrons transfer will be faster than that of the holes. Moreover, the electron effective masses along zigzag and armchair directions of SnP_3 bilayer are almost the same as those of holes. The C^{2D}_α is the in-plane stiffness of 2D structures, where α denotes the zigzag or armchair directions. It can be determined by $C^{2D}_\alpha = [\partial^2 E/\partial\delta^2]/S_0$ (where E is the to-

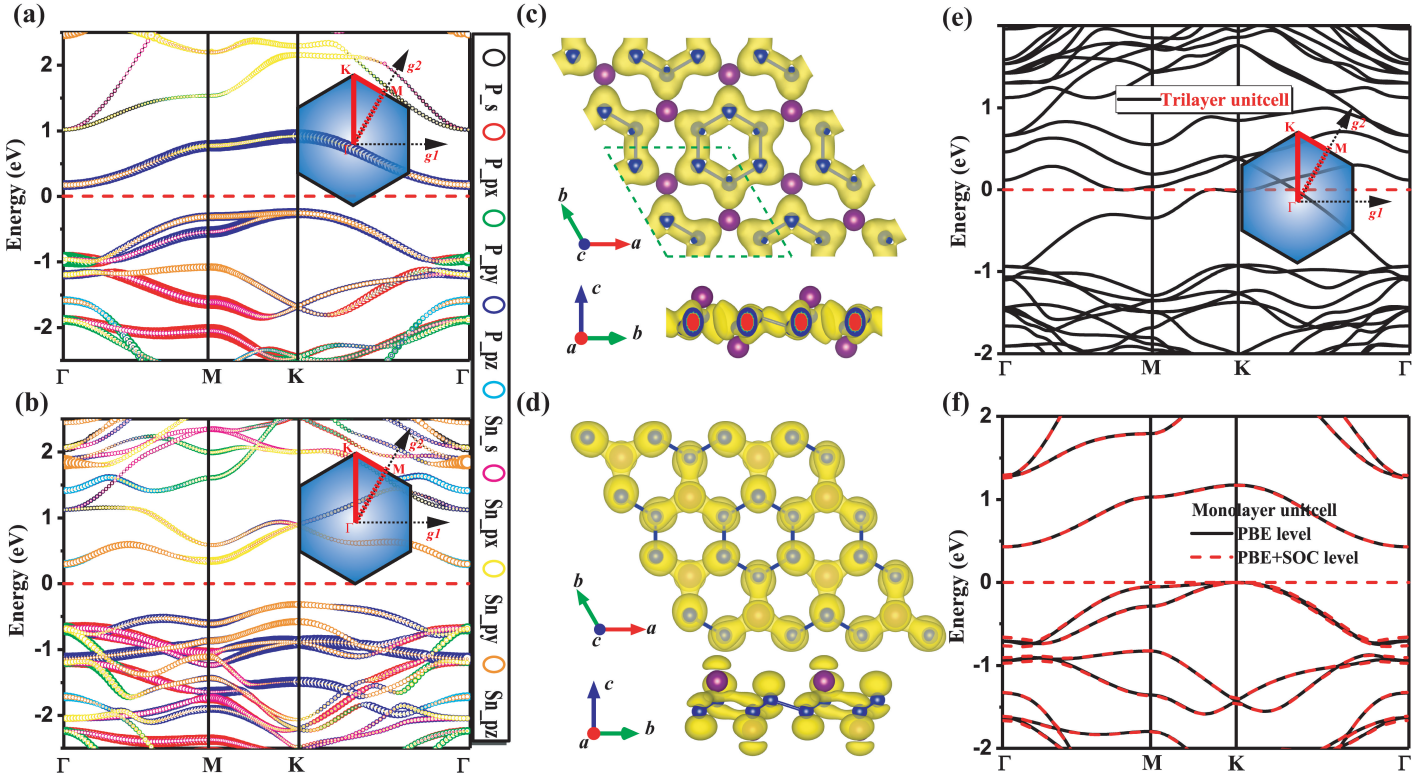

Fig. 4 The orbital-projected band structures of monolayer (a) and bilayer (b) SnP_3 obtained from PBE level in the first Brillouin zone. Inserted is the first Brillouin zone with high symmetric k points: Γ (0,0,0), M (0,0.5,0), and K (-0.333,0.667,0). The energy of Fermi level is set to be 0 eV. Decomposed charge density of VBM (c) and CBM (d) of SnP_3 monolayer at the K and G points are also presented. The isosurface value is 0.003 e/Å^3. (e) The band structure of triplelayer, and (f) the band structure of monolayer with and without SOC effect at PBE level.

tal energy of the 2D structure, S_0 is the area of the equilibrium supercell). The DP constant, E_d^α, is defined by $E_d^\alpha = \partial E_d/\partial\delta$, which denotes the change of the band edges (VBM for holes, CBM for electrons) along different directions activated by strain. Through exerting the compressive and tensile strains δ, the in-plane stiffness C_α^{2D} and the DP constant E_d^α are respectively obtained by parabolic and linearly fitting the data, as demonstrated in Fig. 6. Meanwhile, the exhaustive information of the in-plane stiffness and the DP constants for the SnP_3 monolayer and bilayer along zigzag and armchair directions are listed in Table. 2. The SnP_3 monolayer and bilayer exhibit similar C_{zig}^{2D} and C_{arm}^{2D} in both zigzag and armchair directions (32.96 and 33.00 for monolayer, 93.02 and 92.95 N/m for bilayer), which reveals that the mechanical stress responses of SnP_3 monolayer (bilayer) are isotropic. The phonon-limited carrier mobilities of SnP_3 monolayer and bilayer were evaluated and listed in Table. 2, which illustrates that the carrier mobilities of SnP_3 monolayer along both zigzag and armchair directions have remarkably higher electron mobilities than that of GeP_3 monolayer,[18] owing to the smaller effective masses and larger in-plane stiffness of SnP_3 monolayer. Meanwhile, along both directions, the SnP_3 bilayer possesses much larger hole mobilities respect to the GeP_3 bilayer,[18] while the carrier mobility of electrons are smaller than that of holes due to the relatively larger DP constants along both zigzag and armchair directions.

3.5 Optical properties

The optical absorption properties for SnP_3 monolayer and bilayer were estimated on the basis of the imaginary part $\varepsilon_{\alpha\beta(\omega)}$ of the complex dielectric function $\varepsilon(\omega) = \varepsilon_1(\omega) + i\varepsilon_{\alpha\beta}(\omega)$, which corresponds to the optical absorption at an arbitrary frequency ω. The imaginary part of $\varepsilon_{\alpha\beta(\omega)}$ is defined by the following expression:[57,58]

$$\varepsilon_{\alpha\beta}(\omega) = \frac{4\pi^2 e^2}{\Omega} \lim_{q\to 0} \frac{1}{q^2} \sum_{c,v,k} 2\omega_k \delta(\varepsilon_{ck} - \varepsilon_{vk} - \omega) \times \langle \mu_{ck+e_\alpha} | \mu_{vk} \rangle \langle \mu_{ck+e_\alpha} | \mu_{vk} \rangle^*, \quad (3)$$

where α, β refer to the x, y coordinate directions, and Ω is the volume of the unit cell. The indices c and v represent the conduction and valence band states, respectively. μ_{ck} corresponds to an eigenstate with wave vector k. The absorption coefficient $\alpha(\omega)$ can be calculated by:[59,60]

$$\alpha(\omega) = \sqrt{2}\omega\{\sqrt{\varepsilon_1^2(\omega) + \varepsilon_{\alpha\beta}^2(\omega)} - \varepsilon_1(\omega)\}^{1/2}, \quad (4)$$

where $\varepsilon_1(\omega)$ refers to the real part of the complex dielectric function, which could be obtain from $\varepsilon_{\alpha\beta}(\omega)$ using the Kramer-Kronig relationship.

Using the HSE06 functional, the in- and out-of-plane absorption spectra of the SnP_3 monolayer and bilayer were calculated to investigate their light-harvesting performance, as presented in

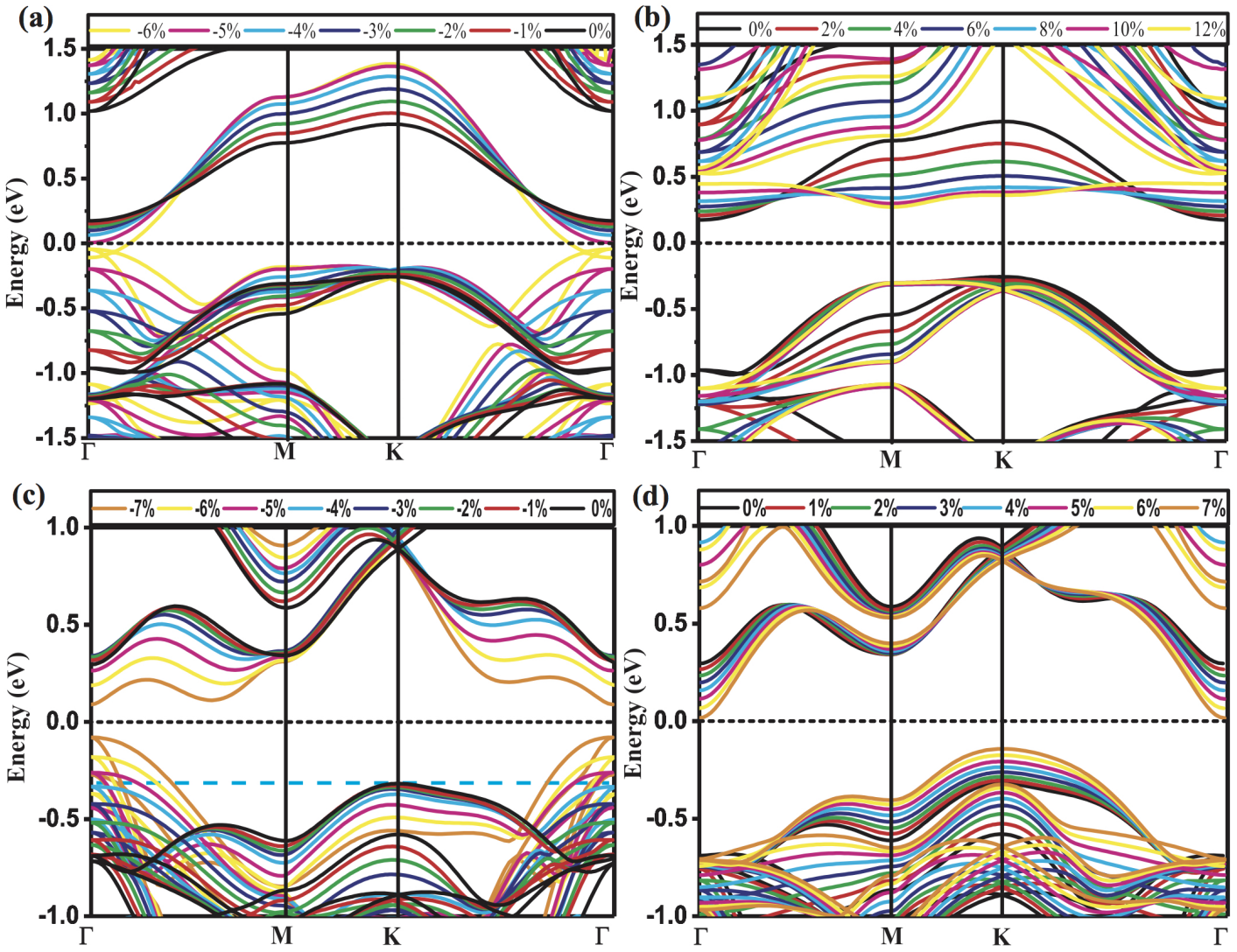

Fig. 5 Band structures of SnP_3 monolayer and bilayer calculated by PBE functional as a function of the compressive (a), (c) and tensile (b), (d) biaxial strains, respectively.

Fig. 7. The absorption coefficients of SnP_3 monolayer and bilayer can reach the order of $\sim 10^6\ cm^{-1}$, which is comparable to organic perovskite solar cells.[61,62] Because of the larger cross-section, the in-plane absorption of the SnP_3 monolayer and bilayer are relatively lager than the corresponding out-of-plane absorption. In addition, compared to the in-plane absorption of SnP_3 monolayer, the SnP_3 bilayer shows excellent absorption because it can absorb and utilize the solar spectra of infrared, visible and near-UV light, while the SnP_3 monolayer mainly absorbs the region between 1 eV and 2 eV, which marks the infrared range of the solar spectra.

4 Conclusions

To summarize, by using first-principle density functional calculations, we theoretically investigate the structural, electronic, mechanical, transport and optical properties of SnP_3 monolayer and bilayer. The phonon dispersion curves and the work function demonstrate that they are both kinetically and chemically stable. The low cleavage energy endorses the possibility of exfoliating them from bulk structure. Analogy to phosphorene, remarkably high carrier mobilities are predicted for SnP_3 monolayer, which is several times higher than that of GeP_3 monolayer. The holes mobilities of SnP_3 bilayer can reach as high as 10^4 $cm^2V^{-1}s^{-1}$. Furthermore, our results revealed that the SnP_3 monolayer and bilayer possess moderate indirect bandgaps and excellent optical properties. The obtained results reveal that SnP_3 monolayer and bilayer have great potential in the applications of microelectronics, optoelectronics and field-effect transistors.

Acknowledgments

The work was supported by the National Natural Science Foundation of China (Grants No. 11774294), the Sichuan Province Applied Science and Technology Project (Grant 2017JY0056), and the Fundamental Research Funds for the Central Universities (2682015QM04). F.C. acknowledges the financial support of NSF DMR 1307740.

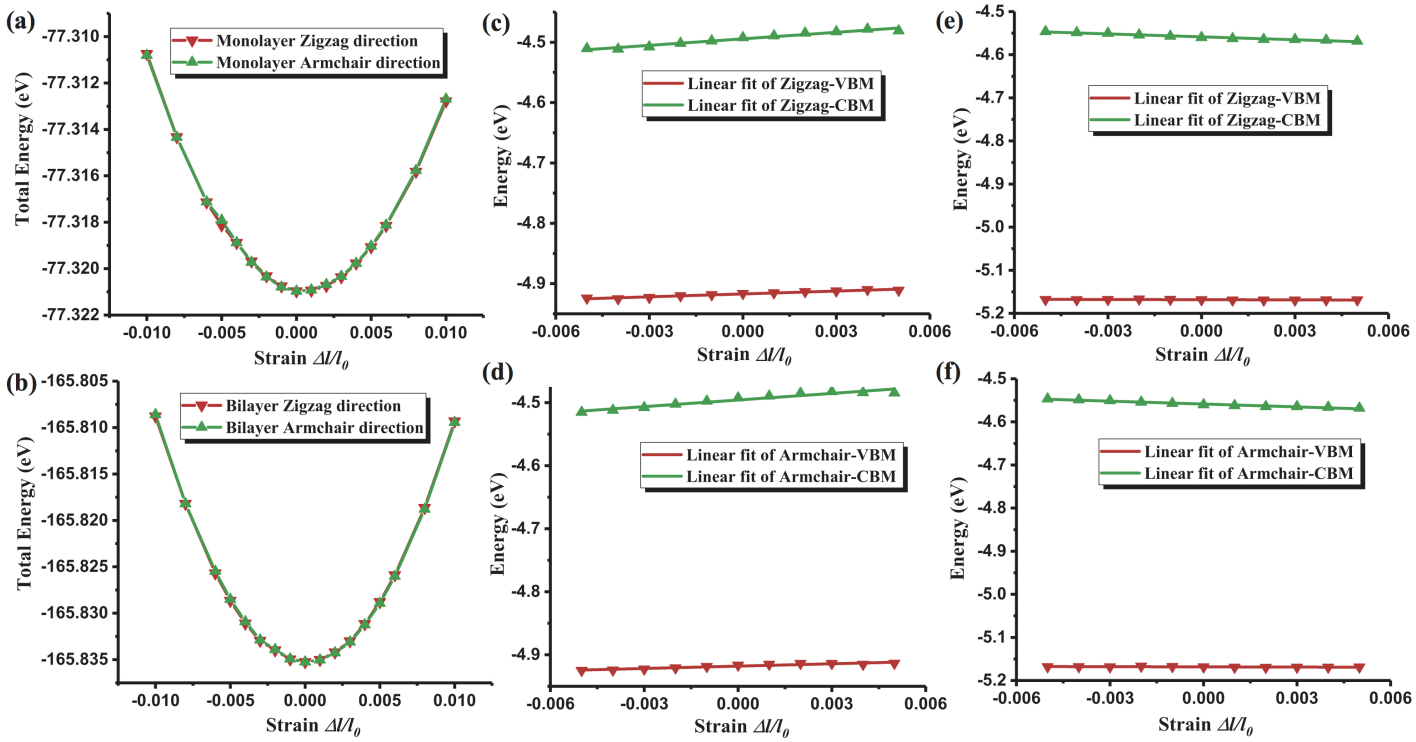

Fig. 6 The relationship between total energy and the applied strain δ along the zigzag and armchair directions. The quadratic fitting of the data gives the in-plane stiffness of 2D structures. The red and green fitting curves in (a) and (b) are shown the in-plane stiffness along zigzag and armchair directions of SnP_3 monolayer and bilayer, respectively.The shift of VBMs and CBMs for the SnP_3 monolayer (c) (d) and bilayer (e) (f) with respect to the vacuum energy as a function of the applied biaxial strain δ along the zigzag and armchair directions, respectively. The linear fit of the data gives the DP constant.

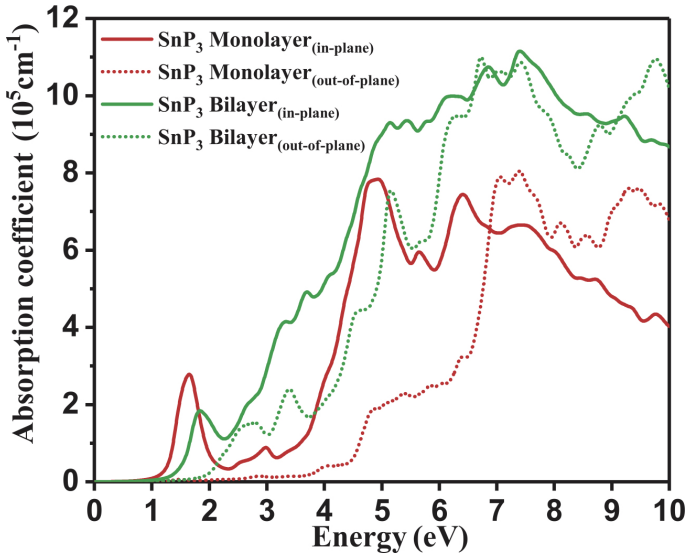

Fig. 7 Calculated light absorption spectra of in- and out-of-plane for SnP_3 monolayer at HSE06 functional level(red solid line and red dashed lines) and bilayer (green solid line and green dashed lines) structures.

References

1 K. S. Novoselov, A. K. Geim, S. V. Morozov, D. Jiang, Y. Zhang, S. V. Dubonos, I. V. Grigorieva and A. A. Firsov, *Science*, 2004, **306**, 666–669.

2 K. S. Novoselov, A. K. Geim, S. V. Morozov, D. Jiang, M. I. Katsnelson, I. V. Grigorieva, S. V. Dubonos and A. A. Firsov, *Nature*, 2005, **438**, 197–200.

3 A. K. Geim and I. V. Grigorieva, *Nature*, 2013, **499**, 419–425.

4 Q. H. Wang, K. Kalantarzadeh, A. Kis, J. N. Coleman and M. S. Strano, *Nat. Nanotech.*, 2012, **7**, 699–712.

5 T. Heine, *Acc. Chem. Res.*, 2015, **48**, 65.

6 C. Jin, F. Lin, K. Suenaga and S. Iijima, *Phys. Rev. Lett.*, 2009, **102**, 195505.

7 A. Nag, K. Raidongia, K. P. Hembram, R. Datta, U. V. Waghmare and C. N. Rao, *Acs Nano*, 2010, **4**, 1539–1544.

8 J. H. Warner, M. H. Rummeli, A. Bachmatiuk and B. Buchner, *ACS Nano*, 2010, **4**, 1299–1304.

9 P. Vogt, P. De Padova, C. Quaresima, J. Avila, E. Frantzeskakis, M. Asensio, A. Resta, G. L. Lay and S. Soleil, *Phys. Rev. Lett.*, 2012, **108**, 155501.

10 E. S. Reich, *Nature*, 2014, **506**, 19–19.

11 E. Bianco, S. Butler, S. Jiang, O. D. Restrepo, W. Windl and J. E. Goldberger, *ACS Nano*, 2013, **7**, 4414–4421.

12 Y. Xu, H. Zhang, H. Shao, G. Ni, J. Li, H. Lu, R. Zhang, B. Peng, Y. Zhu, H. Zhu *et al.*, *Phys. Rev. B*, 2017, **96**, 245421.

13 M. Naguib, V. N. Mochalin, M. W. Barsoum and Y. Gogotsi, *Adv. Mater*, 2014, **26**, 992–1005.

14 K. F. Mak, C. Lee, J. Hone, J. Shan and T. F. Heinz, *Phys. Rev. Lett.*, 2010, **105**, 136805.

15 B. Radisavljevic, A. Radenovic, J. Brivio, V. Giacometti and A. Kis, *Nature Nanotech.*, 2011, **6**, 147–150.

16 L. Liang, J. Wang, W. Lin, B. G. Sumpter, Meunier and M. Pan, *Nano Lett.*, 2014, **14**, 6400–6406.

17 J. Qiao, X. Kong, Z. Hu, F. Yang and W. Ji, *Nat. Commun.*, 2014, **5**, 4475–4475.

18 Y. Jing, Y. Ma, Y. Li and T. Heine, *Nano Lett.*, 2017, **17**, 1833–1838.

19 N. Miao, B. Xu, N. C. Bristowe, J. Zhou and Z. Sun, *J. Am. Chem. Soc.*, 2017, **139**, 11125–11131.

20 F. Shojaei and H. S. Kang, *J Mater. Chem. C*, 2017, **5**, 11267–11274.

21 Z. Zhuo, X. Wu and J. Yang, *Nanoscale*, 2018.

22 J. Gullman and O. Olofsson, *J. Solid State Chem.*, 1972, **5**, 441–445.

23 G. Kresse and J. Furthmuller, *Phys. Lett. B*, 1996, **54**, 11169–11186.

24 G. Kresse and D. P. Joubert, *Phys. Lett. B*, 1999, **59**, 1758–1775.

25 P. E. Blochl, *Phys. Lett. B*, 1994, **50**, 17953–17979.

26 J. P. Perdew, K. Burke and M. Ernzerhof, *Phys. Rev. Lett.*, 1996, **77**, 3865–3868.

27 J. Heyd, G. E. Scuseria and M. Ernzerhof, *J. Chem. Phys.*, 2003, **118**, 8207–8215.

28 J. Heyd, G. E. Scuseria and M. Ernzerhof, *J. Chem. Phys.*, 2006, **124**, 219906.

29 S. Grimme, *J. Comput. Chem.*, 2006, **27**, 1787–1799.

30 H. J. Monkhorst and J. D. Pack, *Phys. Lett. B*, 1976, **13**, 5188–5193.

31 A. Togo and I. Tanaka, *Scr. Mater.*, 2015, **108**, 1–5.

32 S. NosÃľ, *J Chem. Phys.*, 1984, **81**, 511–519.

33 P. Yuan, Z. Zhang, Z. Fan and M. Qiu, *Phys. Chem. Chem. Phys.*, 2017, **19**, 9528–9536.

34 P. Yuan, Z. Fan and Z. Zhang, *Carbon*, 2017, **124**, 228–237.

35 S. Zhang, J. Zhou, Q. Wang, X. Chen, Y. Kawazoe and P. Jena, *P NATL. ACAD. SCI. USA.*, 2015, **112**, 2372–7.

36 L.-Y. Gan and U. Schwingenschlögl, *Phys. Rev. B*, 2014, **89**, 125423.

37 V. Nicolosi, M. Chhowalla, M. G. Kanatzidis, M. S. Strano and J. N. Coleman, *Science*, 2013, **340**, 1226419–1226419.

38 K. S. Novoselov, D. Jiang, F. Schedin, T. Booth, V. V. Khotkevich, S. V. Morozov and A. K. Geim, *Proc. Natl. Acad. Sci. U. S. A.*, 2005, **102**, 10451–10453.

39 Y. Jin, X. Li and J. Yang, *Phys. Chem. Chem. Phys.*, 2015, **17**, 18665–18669.

40 F. Ma, M. Zhou, Y. Jiao, G. Gao, Y. Gu, A. Bilic, Z. Chen and A. Du, *Sci. Rep.*, 2015, **5**, 17558.

41 F. Li, X. Liu, Y. Wang and Y. Li, *J Mater. Chem. C*, 2016, **4**, 2155–2159.

42 Y. Jiao, F. Ma, G. Gao, J. Bell, T. Frauenheim and A. Du, *J Phys. Chem. Lett.*, 2015, **6**, 2682–2687.

43 S. Zhao, Z. Li and J. Yang, *J. Am. Chem. Soc.*, 2014, **136**, 13313–13318.

44 I. B. Bersuker, *Chem. Rev.*, 2001, **101**, 1067–1114.

45 S. Zhang, Z. Yan, Y. Li, Z. Chen and H. Zeng, *Angew. Chem.*, 2015, **54**, 3112–3115.

46 Y. Li and Z. Chen, *J. Phys. Chem. C*, 2014, **118**, 1148–1154.

47 B. Amin, T. P. Kaloni and U. Schwingenschlogl, *RSC Adv.*, 2014, **4**, 34561–34565.

48 Y. Y. Hui, X. Liu, W. Jie, N. Y. Chan, J. Hao, Y. T. Hsu, L. Li, W. Guo and S. P. Lau, *ACS Nano*, 2013, **7**, 7126–7131.

49 K. He, C. Poole, K. F. Mak and J. Shan, *Nano Lett.*, 2013, **13**, 2931–2936.

50 Z. Wang, X.-F. Zhou, X. Zhang, Q. Zhu, H. Dong, M. Zhao and A. R. Oganov, *Nano. Lett.*, 2015, **15**, 6182–6186.

51 L. Zhang, G. Qin, W. Fang, H. Cui, Q. Zheng, Q. Yan and G. Su, *Sci. Rep.*, 2016, **6**, 19830.

52 J. Bardeen and W. Shockley, *Phys. Rev.*, 1950, **80**, 72–80.

53 S. Bruzzone and G. Fiori, *Appl. Phys. Lett.*, 2011, **99**, 222108.

54 J. Chen, J. Xi, D. Wang and Z. Shuai, *J Phys. Chem. Lett.*, 2013, **4**, 1443–1448.

55 J. Dai and X. C. Zeng, *Angew. Chem. Int. Ed.*, 2015, **54**, 7572–7576.

56 S. Zhang, M. Xie, F. Li, Z. Yan, Y. Li, E. Kan, W. Liu, Z. Chen and H. Zeng, *Angew. Chem. Int. Ed.*, 2016, **128**, 1698–1701.

57 T. Korn, S. Heydrich, M. Hirmer, J. Schmutzler and C. Schüller, *Appl. Phys. Lett.*, 2011, **99**, 102109.

58 D. Xiao, G.-B. Liu, W. Feng, X. Xu and W. Yao, *Phys. Rev. Lett.*, 2012, **108**, 196802.

59 S. Saha, T. Sinha and A. Mookerjee, *Phys. Lett. B*, 2000, **62**, 8828.

60 X. Zhang, X. Zhao, D. Wu, Y. Jing and Z. Zhou, *Adv. Sci.*, 2016, **3**, 1600062.

61 N. J. Jeon, J. H. Noh, Y. C. Kim, W. S. Yang, S. Ryu and S. I. Seok, *Nat. Mater.*, 2014, **13**, 897–903.

62 M. Shirayama, H. Kadowaki, T. Miyadera, T. Sugita, M. Tamakoshi, M. Kato, T. Fujiseki, D. Murata, S. Hara, T. N. Murakami *et al.*, *arXiv: Materials Science*, 2016, **5**, 014012.

TOC figure

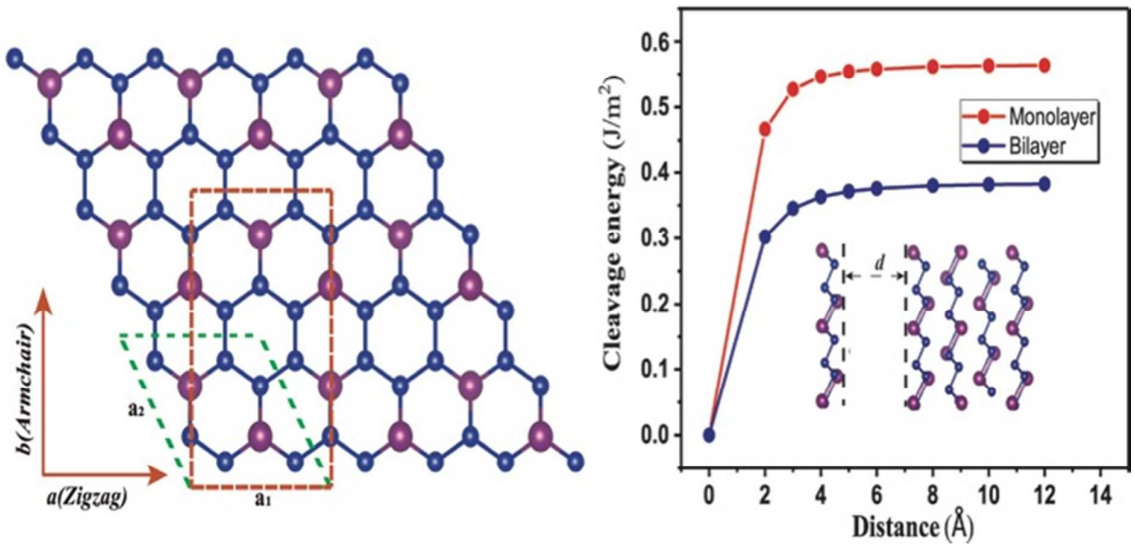

A novel semiconducting 2D material based on SnP_3 monolayer and bilayer is proposed by first-principles calculations.